

**Results of FDA's First Interlaboratory Computational Study
of a Nozzle With a Sudden Contraction and Conical Diffuser**

Sandy F.C. Stewart¹, Prasanna Hariharan¹, Eric G. Paterson², Greg W. Burgreen³,
Varun Reddy², Steven W. Day⁴, Matthew Giarra⁴, Keefe B. Manning²,
Steven Deutsch², Michael R. Berman¹, Matthew R. Myers¹, Richard A. Malinauskas¹

¹*Food & Drug Administration*

²*Pennsylvania State University*

³*Mississippi State University*

⁴*Rochester Institute of Technology*

Address for Correspondence: Sandy F.C. Stewart, Office of Science and Engineering
Laboratories, Food and Drug Administration, 10903 New Hampshire Ave., Bldg 62, Rm 2210,
Silver Spring MD 20993. Tel: 301-796-2518. Fax: 301-796-9932. E-mail:
sandy.stewart@fda.hhs.gov

Abstract

The U.S. Food and Drug Administration recently hosted an interlaboratory study to assess the suitability and methodology of computational fluid dynamics (CFD) for demonstrating medical device safety in regulatory submissions. The benchmark study was performed in a generic medical device consisting of a 0.012 m diameter cylindrical nozzle with a sudden contraction and 10° conical diffuser, on either side of a 0.04 m long, 0.004 m diameter throat. Results from 28 simulations from around the world were compared to planar particle image velocimetry (PIV) measurements performed at three laboratories. Five flow rates were chosen that produced laminar, transitional, and turbulent regimes. In general, the CFD results showed modest agreement in global and local flow behaviors. However, all CFD data sets contained wide degrees of velocity variation in comparison to experiment and with each other, much of which could be attributed to the turbulence models used. Some of the velocity discrepancies in the sixteen three dimensional (3D) simulations resulted from substantial flow asymmetries within and downstream of the conical diffuser. Large differences in velocity symmetry were found even when using the same code and many of the same simulation parameters. In contrast, no velocity asymmetries of the same magnitude were observed in any of the planar PIV experiments; relatively minor asymmetries in one experiment were linked to slight asymmetries in the velocity profile at the inlet to the nozzle. CFD predictions of peak wall shear stress at the sudden contraction (normalized to that 0.02 m downstream) varied over two orders of magnitude, with variations of greater than 10 times even when the same software and turbulence model were used. This degree of shear stress variation will necessarily propagate through calculations of blood damage in medical devices. We conclude that CFD simulations used in qualifying medical devices for regulatory purposes need to be conducted following the best practices

available, and that targeted experimental validation is essential. The results of this interlaboratory study are freely available in an internet repository (<https://fdacfd.nci.nih.gov>).

We encourage the use of this model in further studies, and support the development of additional benchmarks, better modeling techniques, and consensus standards and guidelines for using CFD in the evaluation of medical devices.

Key Words: CFD validation, standards, medical device regulation, best practices, blood flow.

Introduction

Computational fluid dynamics (CFD) is a popular tool used to study and develop complex medical devices such as endovascular stents,⁶ cannulae,⁸ prosthetic heart valves,^{23,35,37} and ventricular assist devices.^{26,36} However, the usefulness of CFD in assessing safety in a way that can facilitate the regulatory process has received less study. In the cardiovascular area, the main fluid component of interest is blood, which is extremely difficult to model. The ~50% cellular content can still only be fully modeled at limited scale sizes, while the full chemistry of coagulation is as yet too complex to be modeled without significant simplifications. One technique used to evaluate blood damage, such as hemolysis, is by assessing the effects of shear stress and exposure time in a continuum fluid. Most blood damage models depend on empirical shear stress/exposure time data gathered decades ago. However, if the physics of the continuum blood flow is not modeled correctly, then the computed biological effects cannot be trusted.²⁰ Therefore, this interlaboratory study had three main goals: 1) to take a snapshot of the current practice in medical device fluid dynamics computations, 2) to compare hemolysis levels predicted by the computations, and 3) provide benchmark models for validation work in the medical device arena. In this paper, we concentrate on goal #1.

This is a continuation of our earlier work which evaluated flow through the nozzle in the opposite direction, through a conical concentrator and sudden expansion.³¹ In that paper, we found variations in velocities relative to the experiments that depended primarily on the turbulence models used. Recirculation in the post-expansion region was difficult to model at the higher Reynolds numbers. No one turbulence model proved superior overall when applied to this problem. We also found wide variations in shear stress distributions (particularly the wall shear stress). As mentioned above, this has particular relevance for blood damage modeling: if

the shear stresses cannot be accurately predicted, then reliable and accurate numerical prediction of shear-induced blood damage cannot be performed. We noted that higher mesh densities did not necessarily provide better match to the velocities; thus careful experimental validation is needed, with monitoring of shear stresses in areas relevant to blood damage. We found no particular correlation between self-rated expertise and accuracy, and we concluded that there was little uniformity of practice among the 28 users. CFD modeling of an actual device must take into consideration many complications: short and/or curved entrance and exit conduits, pulsatile flow, transitional flows, secondary flows, sharp corners, and a range of viscosity and hematocrit under which the device is used. We concluded that CFD can be a useful part of regulatory evaluations, but that successful computational simulation of this nozzle model will not aid in a regulatory submission where the model is not applicable.

The current geometric configuration allowed for the examination of CFD performance in an environment of a continuously varying adverse pressure gradient, present in the conical diffuser. The diffuser geometry allowed investigation into how different models predicted flow separation at different locations in the presence of the adverse pressure gradient, which may be relevant to any device where flow decelerates. Likewise, the sudden contraction, not studied in the first paper, is relevant to implants containing small orifices, such as gaps between heart valve leaflets, or to diameter mismatches between cannulae and dialysis tubing. Regions just upstream of the sudden contraction are challenging locations for the computation of wall shear stress, which are important for hemolysis computations. The actual hemolysis calculations, part of goal #2, will be detailed in a future report. Data from this study is available on our website, <https://fdacfd.nci.nih.gov>, and is already being used in benchmark studies (goal #3).^{3,9,10,15,17,34,38}

Methods

Participants in the computational interlaboratory study were asked to model flow in a generic example of a tubular medical device containing a sudden contraction and conical diffuser (Figure 1), similar to models used previously (e.g., Umezu et al.,³² Hinds et al.¹⁸). This model shares flow characteristics with some common medical devices (e.g., catheters, needles) and medical device problems (e.g., kinks in dialysis tubing). Nozzle throat Reynolds numbers (Re_t) were specified at 500, 2000, 3500, 5000, and 6500 under steady flow conditions. A Newtonian viscosity of $0.0035 \text{ N}\cdot\text{s}/\text{m}^2$ and a density of $1056 \text{ kg}/\text{m}^3$ were specified. All other parameters (inlet/outlet lengths, mesh density, cell/element type, axisymmetric vs. 3D mesh, inlet boundary conditions, etc.) were left to the discretion of the individual participants. More details of the interlaboratory study can be found in our previous report,³¹ and at our data repository website, <https://fdacfd.nci.nih.gov>.

The CFD simulations were compared to experimental data obtained using 2D planar particle image velocimetry (PIV) in machined and polished acrylic nozzles as described previously.¹⁶ Steady flow velocities were measured at the cross-sectional model locations shown in Figure 1b, at three separate laboratories (two experimental data sets obtained at one lab, one each at the other two labs). The nozzle models were fitted with straight inlet tubes $\sim 1.20 \text{ m}$ long (~ 100 tube diameters) to ensure fully developed flow at the nozzle inlet. Outlet tubes $\sim 1.0 \text{ m}$ long were also used to prevent outlet flow conditions from influencing the reattachment point in the model.

The fluid used in the PIV experiments was composed of 50 wt % saturated sodium iodide (NaI) solution, 20 wt % glycerin, and 30 wt % water, formulated to match the index of refraction of the acrylic nozzles (~ 1.49) used in the experimental flow loops. The range of dynamic

viscosity and density was equal to $1.66\text{-}1.77 \times 10^3 \text{ kg/m}^3$ and $6.74\text{-}7.77 \times 10^{-3} \text{ N s/m}^2$, respectively. To ensure proper control of the flow conditions, the dynamic viscosity and density of the fluid were measured before each PIV measurement. The flow rate was adjusted according to the fluid property variations to match the specified throat Reynolds numbers. The PIV measured velocities were then scaled to those in the computational simulations using dynamic similarity.¹³ All axial velocities (PIV and CFD) were then normalized by the mean axial velocity calculated from the velocity profile at the inlet (Figure 1b, location 1, $z = -0.048$):

$$u_z^* = \frac{u_z}{\bar{u}_z} \quad (1)$$

In equation 1, u_z^* = normalized velocity, u_z = velocity from PIV or CFD, and \bar{u}_z = average velocity at the inlet, calculated as follows:

$$\bar{u}_z = \frac{Q_{inlet}}{A_{inlet}}, \quad (2)$$

where Q_{inlet} = flow rate at the inlet (calculated from the velocity profile determined from PIV or CFD), and A_{inlet} = area of the 0.012 m diameter inlet tube.

Pressures were validated against measurements made in a separate wall pressure tap model mounted in the same flow loop, using an aqueous glycerin solution. Measured pressures were converted to those of the simulations by the following equation to preserve similarity according to the Euler number:

$$P_b = P_g \frac{\rho_b \bar{u}_b^2}{\rho_g \bar{u}_g^2}, \quad (3)$$

where P = pressure, ρ = density, \bar{u} = axial velocity at inlet averaged over inlet area, and subscripts b and g refer to blood and glycerin, respectively.¹⁶ All the CFD and experimental pressure values were normalized by the downstream value at axial coordinate $z = 0.09032 \text{ m}$.

Results

Axial velocity along nozzle centerline

At $Re_t = 500$, the experiments showed that the normalized axial velocity along the centerline increased abruptly at the sudden contraction (Figure 2a), continued to increase within the nozzle throat as the flow developed, then slowly decreased as a function of axial position within the conical diffuser. A jet formed within the conical diffuser associated with low velocity recirculation zones at the wall (the diffuser angle being too large to smoothly diffuse the flow at this Re_t), and the jet widened and slowed as the diffuser area increased with axial position downstream. While the PIV results demonstrated good interlaboratory comparability, the results from the simulations showed a high degree of variation. Many of the participants used turbulence models (including variations of k-epsilon, k-omega, and shear stress transport models) at $Re_t = 500$, even though this is below the critical Reynolds number for pipe flow. The wide degree of variation of results (and use of turbulence models at $Re_t = 500$) was also observed in the nozzle model when oriented with the sudden expansion at the exit (the Sudden Expansion orientation).³¹ Axial velocities predicted by many of the k-omega/shear stress transport (SST) models matched those of the experiment well, but only up to a point, then abruptly fell off between 0.08 and 0.12 m downstream of the sudden contraction. However, even some of the laminar simulations did not accurately predict the centerline axial velocity. Two of the poorly performing laminar models (labeled #1 and #3 in Figure 2a) used outlet lengths that were likely too short for the flow to develop properly for the outlet boundary conditions used. Triangular and tetrahedral cells are thought to be less accurate for CFD than quadrilateral and hexahedral cells of the same size, and indeed some of the poorly performing laminar simulations used triangular cells (#1, #3, and #5) or tetrahedral cells (#2 and #4). However, some of the other

triangle and tetrahedral simulations performed better. Other than the short outlet length, however, the problems in the laminar simulations were not readily identifiable.

At $Re_t = 2000$ in the experiments (Figure 2b), flow was observed to be laminar within the inlet and nozzle throat, and transitional within the cone and outlet. The jet broke down within the outlet tube, the location of which varied considerably among the simulations. The one Spalart-Allmaras (SA) model matched the centerline velocity well, while the SST and k-omega (KO) models performed better than the k-epsilon (KE) models. There was considerable variation among the SST, KO, and KE models.

The KE and SST models appeared to bracket the experimental centerline velocity as the Re_t increased (Figure 2c and d). At $Re_t = 6500$, the various SST models matched the throat centerline velocity better than did the KE models, while the reverse was true within the diffuser. In contrast, in the Sudden Expansion orientation, the SST models always performed better in the nozzle throat and downstream of the sudden expansion, although the KE models approached the SST models as Re_t increased.³¹ At all Re_t (including $Re_t = 5000$, not shown) there was little overlap between the KE and SST models. In general, the SST models tended to transition to turbulence farther downstream than did the KE models, but they did not necessarily do better in matching the centerline velocities at all Re .

Pressure variations

Figure 3a-d shows the wall pressures, as well as the pressures along the centerline (insets). Two to three simulations per Re_t were omitted due to formatting errors in the datasets that could not be corrected. For comparative purposes, the pressures for each case (simulation and experimental) were referenced to that at $z = 0.09032$ m, the most downstream point measured in the wall tap experimental model (location 12 in Figure 1b). As expected, both the

simulations and experiments showed higher pressure gradients in the small diameter throat than in the inlet and outlet tubes. An adverse pressure gradient at the wall was predicted in many cases just downstream of the sudden contraction, due to the presence of a vena contracta (seen experimentally at Re_t greater than 500, Figure 3b, c, d). An adverse pressure gradient was also found within the diffuser as the fluid separated from the wall, with low velocities in recirculation zones. The inset pictures in Figure 3 show the simulated centerline pressures. The most noticeable difference between the simulated wall and centerline pressures is apparent just downstream of the sudden contraction ($z \geq 0.0$ m), where the wall pressure was somewhat lower than the centerline pressure in many simulations. As flow enters a sudden contraction, the velocities are higher near the wall (as the flow accelerates around the corner), but lower at the centerline. The flow typically separates, forming a small recirculation zone (Figure 3e), with a corresponding increase in wall pressure. Just downstream of the sudden contraction, the centerline velocity increases as the flow develops. Contour images supplied by participants (not shown, but available at <https://fdacfd.nci.nih.gov>) suggest that these recirculation zones may not have been resolved in some of the simulations, particularly if turbulent wall functions with a large cell size in the near-wall layer were used.

Volumetric flow rate

Volumetric flow rates were calculated by integrating over the axial velocity profiles at each of the 12 cross-sectional cuts, to give a conservation of mass error metric as a function of axial position z (Figure 4):³¹

$$E_Q = \frac{Q_{CFD} - Q_{theory}}{Q_{theory}} \times 100\% \quad (4)$$

where Q_{CFD} = the volumetric flow rate computed from the CFD axial velocity profiles, and Q_{theory} = theoretical volumetric flow rate calculated from the throat Reynolds number and

diameter. For axisymmetric meshes, Q_{CFD} was calculated from zero radius to the outer radius of the nozzle, along each of the twelve axial velocity profiles. For 3D meshes, Q_{CFD} was calculated across the diameter. The radius was dependent on location (inlet, outlet, throat, or cone). A simple Riemann sum in the radial direction was used for the numerical integration. When compared to the theoretical flow rate, a considerable degree of variation was observed in a number of the simulations, as well as in some of the experiments. In addition, several 3D simulations demonstrated substantial flow asymmetries within the conical diffuser, causing errors in the flow rate calculated from equation 4, which assumes symmetric flow.³¹ The asymmetries were likely due to instabilities resulting from the adverse pressure gradient visible within the conical diffuser in Figure 3. To differentiate conservation of mass errors from asymmetries, only the errors upstream of the diffuser were evaluated (i.e., locations 1-3 and 5-7 in Figure 1b). Mass conservation errors at the sudden contraction (location 4, $z = 0$ m) were also neglected because of errors in extracting data from the participants' solutions, giving non-zero interpolated velocities along the perpendicular wall of the sudden contraction. Examples of such errors are visible in panel c of Figure 6 - Figure 9, which show non-zero velocities beyond the wall at the throat radius ($r < -0.002$, $r > 0.002$ m) in some of the data. Errors in the experiments at $z = 0$ m were due to suboptimal visualization through the perpendicular wall at the sudden contraction, and due to residual machining marks.

Flow asymmetry

Flow asymmetry in the 3D simulations was characterized by calculating the ratio of the volumetric flow rate (calculated as described above) on one side of the centerline to the other, to produce a number ≤ 1.0 , with a value of 1.0 indicating perfect symmetry¹⁶ (Figure 5). The degree of asymmetry was highly variable from simulation to simulation, and reached negative

values in some cases (representing net negative flow on one side of the centerline). Asymmetries developed within the conical diffuser, but resolved further downstream. Asymmetries were also calculated from the experiments, but were lower in magnitude than in the simulations. We return to this subject below, and in the *Study limitations* section.

Axial velocity profiles

For clarity, the figures in this section are limited to the 64-68% of the simulations with conservation of mass errors $\leq 10\%$ upstream of the conical diffuser. At $Re_t = 500$, the experimental axial velocity profiles demonstrated laminar flow throughout the nozzle, as would be expected from the low Reynolds number at the model inlet (e.g., $Re_{inlet} = 167$ for $Re_t = 500$, Figure 6a). Despite many of the participants submitting turbulent simulations, most of the simulations were able to accurately predict velocity in the nozzle inlet (Figure 6a and b) and throat (Figure 6d and e). However, all of the simulations underestimated the velocities by about 25% in most of the central area of the sudden contraction (Figure 6c), with some overestimation near the wall (also note the low calculated flow rates at $z = 0$ in Figure 4a). As mentioned above, a few of the simulations showed non-zero velocities at radii greater than 0.002 m, possibly due to errors in data extraction. Within and downstream of the diffuser (Figure 6f through i), simulations using the KE models diverged markedly from measurements, while the laminar, KO, and SST models generally performed better, even predicting the recirculation zones in the diffuser and just downstream (Figure 6f, g, and h). One of the laminar simulations did poorly, however, possibly due to too-short an outlet length. Further downstream, nearly all of the turbulent simulations performed poorly (Figure 6h and i).

At $Re_t = 2000$, many of the simulations did not accurately predict the parabolic velocity profile at the inlet observed in the experiments (Figure 7a). Interestingly, three of the SST

simulations performed better than two of the laminar simulations. In the throat, the predictions were fairly good (Figure 7d and e); however, the central velocities were again underestimated by all the simulations at the sudden contraction (Figure 7c). In the diffuser, the turbulent models began to fail, with the KO and KE models performing worse than the SST and SA models (Figure 7f and g). Just downstream of the diffuser (Figure 7h), only the laminar simulations matched the measurements; however, further downstream the experimental jets were observed to be in transition, so that the turbulence models performed better than the laminar simulations (Figure 7i). Thus the quality of prediction of mean velocities in the transition to turbulence is very much dependent on the Reynolds number, the position of the jet breakdown, and the turbulence model used. Furthermore, the KO model (a steady flow 3D study with hexagonal elements) showed a striking asymmetry that was not observed in the experiments or other simulations (Figure 7f-i).

At $Re_t = 3500$, the inlet flow was observed to be laminar, while most of the turbulent models assumed a turbulent velocity profile (Figure 8a and b). Predictions at the sudden contraction followed trends similar to $Re_t = 500$ and 2000. Errors in one of the experimental profiles caused large confidence intervals on one side. Within the nozzle throat, the SST models predicted the flow profiles fairly well (Figure 8d and e). The SST, SA, and laminar models performed well in the diffuser, while the KE simulations began to fail there (Figure 8f and g). Obvious flow asymmetries were observed in some cases, in the diffuser and outlet (Figure 8f-i).

At $Re_t = 6500$ (Figure 9), the flow rate in one set of experiments was 10% too high, which tripped the flow at the inlet from the laminar to the turbulent regime; the other experiments were laminar at the inlet (Figure 9a). (This experimental error resulted in the larger confidence intervals in Figure 9). Among the simulations, similar results to $Re_t = 3500$ were

found; only the laminar simulation predicted a parabolic inlet velocity profile. Inconsistent CFD predictions were found with the turbulent models overall, with the SST models performing better than the others in the inlet and throat (Figure 9a-e), and the KE models performing better in the diffuser and outlet (Figure 9g-i). Again, several of the simulations showed marked asymmetries in the outlet. These trends were also seen at $Re_t = 5000$ (not shown).

Similar simulation parameters can lead to markedly different levels of asymmetry. Two such cases are compared in Figure 10. The axial velocity profiles oriented at 0° , 45° , 90° , and 135° are plotted for $Re_t = 6500$, just downstream of the conical diffuser ($z = 0.072$ m, location 10 in Figure 1b). The parameters for both simulations are shown in Table 1. Despite many similarities -- same code, same turbulence model (SST), same cell shape (hexahedral) -- only one of the two simulations showed patently asymmetric flow. Figure 10 also shows the meshes used in the two simulations, as well as the user-provided color velocity contour plots, with the locations of the velocity contours superimposed. One significant difference between the two simulations is that the symmetric study was performed in steady flow, while the asymmetric one was a transient study. However, the asymmetric KO results observed at $Re_t = 2000$, 3500 , and 6500 in Figure 7 - 9 (as well as at $Re_t = 5000$, not shown) were from simulations performed under steady flow conditions, using a hexahedral mesh. Thus steady vs. transient conditions cannot be the sole reason for the difference.

Wall shear stress (WSS)

For clarity, the figures in this section are limited to simulations with conservation of mass errors $\leq 10\%$. Computational shear stress magnitudes, $|\tau|$, were requested from participants performing simulations, and defined as:³¹

$$|\tau| = 2.0\mu\sqrt{S_{ij}S_{ij}} , \quad (5)$$

where S_{ij} = components of strain-rate tensor, μ = dynamic viscosity, and repeated indices indicate summation. Computed wall shear stress values along the nozzle are shown in Figure 11. CFD data was requested from participants as a function of axial distance only, so that, in 3D simulations, the angular position (θ) on the wall was not known. Figure 11a shows all CFD data for $Re_t = 500$; for clarity, the remaining panels only show 0.5% of the data points, because some of the variations in WSS with θ were large enough to obscure the rest of the data. In general, the most consistent simulations were those using SST models; however, even within the SST models, the variations in WSS within the nozzle throat appeared to increase with Re_t . Salient features include a sharp peak in WSS at the sudden contraction, as well as a local minimum just downstream of the contraction as evidence of a recirculation zone.

Wall shear stress values estimated from PIV were not reported in Figure 11 because the inter-laboratory variability in the experimental WSS was very high ($\sim 100\%$). The primary reason for the large variability in PIV WSS was inadequate spatial resolution in the PIV images which prevented us from resolving the viscous sub-layer (near wall region), especially for turbulent flows. In addition, the presence of large near-wall velocity gradients and the uncertainties involved in identifying the exact wall-location also contributed to the measurement uncertainty. Previous studies have shown that some of these issues could potentially be addressed using high resolution images and by using special near-wall algorithms that minimize the imaging and gradient artifacts.^{12,19,22,24,33} With PIV being used as a common validation tool for CFD, our future studies will focus on addressing some of these issues in an effort to improve the accuracy of WSS measurements.

Variations in the WSS results from only the SST models are shown in greater detail in Figure 12, which compares simulations using two commercial CFD codes (codes A and B). In

this figure, the WSS has been normalized to the value at $z = 0.015$ m (i.e., 0.015 m downstream of the sudden contraction and within the throat region). The location of the reattachment point (indicated by the minimum WSS) as well as the size of the peak WSS at the sudden contraction varied considerably from simulation to simulation, despite the use of the same CFD code. See Table 2 for details of the simulations presented in Figure 12a. The information in Table 2 reveals no obvious relationship between the simulation parameters and the variations in reattachment point location or peak WSS.

Discussion

Many of the same observations reported here for CFD simulations of the Conical Diffuser orientation of the nozzle interlaboratory study were also made for the Sudden Expansion orientation, including the wide variety of methods used, common errors made, and variations in results obtained.³¹ The most obvious error appeared to be the use of turbulence models at $Re_t = 500$, where experimentally the flow was observed to be laminar throughout. At higher Re_t , the experimental flows were observed to be laminar at the inlet, with a transition from laminar to turbulent flow occurring at the sudden contraction. Thus both the laminar simulations, which assumed laminar flow everywhere, and the turbulence models, which assumed turbulent flow everywhere, had difficulty predicting the velocities over the entire computational domain. At $Re_t = 3500$, three of the SST models (Figure 8, red dashed lines) performed well throughout the domain, with realistic parabolic input profiles, blunted flow within the throat, and accurate recirculation zone predictions within the diffuser. Two of these three SST simulations were axisymmetric (with quadrilateral cells), both using the same commercial program. The one 3D simulation used hexahedral cells and a second commercial

program. The 3D simulation and one of the axisymmetric simulations did not use wall functions. The minimum cell size varied from 1.2×10^{-13} to 7.9×10^{-9} m, and the number of cells varied from ~52000 for the two axisymmetric simulations to 1.4×10^6 for the 3D simulation. Thus, these three SST simulations with good results were obtained using a variety of methods. In contrast, *all* of the KE models at $Re_t = 3500$ (Figure 8, blue dash-dot lines) underpredicted the central flow everywhere except for the downstream region of the throat and the outlet (Figure 8e and i). The SST models were less successful at $Re_t = 6500$. Because there are so many variables that could influence the results, any two simulations may predict similar results for vastly different reasons. Thus there is no one-size-fits-all solution for this particular problem and range of flow rates, emphasizing the need for making well-informed choices in simulations. Such variation among turbulence models (albeit at higher Reynolds numbers) have been observed in diffusers in previous studies.^{1,21}

Conservation of mass did not appear to be obeyed in some of the simulations; we also observed this in the Sudden Expansion orientation.³¹ This may in part be due to data interpolation/extraction errors, an obvious example of which can be seen at the sudden contraction itself (Figure 6c), where velocities at the wall should be zero due to the no-slip condition. Any non-zero velocities interpolated erroneously to the wall of the sudden contraction ($r < -0.002$ m, $r > 0.002$ m) were neglected in our volumetric flow rate calculation, and thus contributed to some of the low flow rates at $z = 0.0$ m in Figure 4. Although this did not explain all the errors (there were far fewer flow rate errors at the sudden expansion with flow going in the opposite direction³¹), it does suggest that extrapolation/interpolation errors within the flow domain may have contributed to violations of the conservation of mass.

Several of the 3D simulations of the Conical Diffuser nozzle configuration showed

significant flow asymmetries developing in the area of adverse pressure gradient in the diffuser, despite the symmetric geometry and flow inlet boundary conditions. Similar asymmetries have been reported in laminar flow in symmetric sudden expansions and diffusers, both experimentally^{7,11} and numerically.^{23,27} The asymmetries observed in the 3D simulations of this study may have resulted from the evolution of the unstable flow through the adverse pressure gradient in the diffuser. This decelerating flow is highly sensitive to any perturbations generated by mechanisms such as round-off errors or mesh nonuniformities. The sudden contraction geometry just upstream is an additional complication not included in earlier studies.

Complex unsteady flows due to flow instabilities in areas of adverse pressure gradients have also been found in computational and experimental models of a total cavopulmonary connection in repair of single ventricle heart disease,³⁰ in which four vessels are surgically connected into a cross-shaped junction, with two inflow branches (superior and inferior vena cava) and two outflow branches (right and left pulmonary arteries). Good agreement in global results (control volume power losses) were found between experiment and steady simulations, but accurate description of the detailed velocity field required a second-order accurate unsteady solution on a very fine computational mesh that could resolve (but not exactly duplicate) the disturbed flow in the center of the junction.³⁰ In the current study, global pressure drops across the model were successfully captured in many cases despite suboptimal predictions of velocity and shear stress. Note that we did not request data about whether unsteady simulations were performed as first-order, second-order, or hybrid; this would be good candidate data to collect in future interlaboratory studies. Whether this level of detail is necessary for evaluating computational studies in regulatory submissions is unknown.

Some of the PIV experiments also showed minor flow asymmetries that were much less

significant than most of those of the computational simulations and were attributed to slight inlet flow asymmetries. Experimental flow asymmetries may also have been due to imperfect axial alignment of the inlet tubing, nozzle throat, cone, and outlet sections of the acrylic models (although detailed standard operating procedures were in place to minimize these¹⁶). Numerical artifacts leading to asymmetries may have included asymmetric, non-flow-aligned meshes (e.g. tetrahedral meshes) that produce asymmetric regions of artificial dissipation, or characteristics associated with specific turbulence models. For unsteady calculations, such instabilities may arise as a transient start-up anomaly and persist for an unexpectedly large number of time steps before ever convecting out of the domain. Numerical round-off errors in the geometry, mesh, and solvers (including the turbulence models used) may also have contributed to instabilities. Because of the unstable nature of decelerating flow, even minor perturbations occurring in a perfectly symmetric situation (whether experimental or numerical) can be amplified leading to visible asymmetries. Asymmetries are likely to occur in medical devices due to transient flow pulses, changes in flow geometries, and curvature effects. Therefore, we contend that in both computations of flow in medical devices, and in experimental validations thereof, vigilance is needed to identify and understand instabilities and asymmetries, and to carefully assess their real-world importance.

Flow of blood past corners and edges is a concern because of the possibility of high shear stresses in these areas. In this nozzle model, the sudden contraction is the location of the highest shear stresses and is the prime location where blood damage and/or platelet activation might occur. This is especially true near the wall, where the shear stress is high but the absolute velocities are low, so that the exposure time is also high (although less fluid volume would be expected to be exposed because of the lower velocities). Furthermore, the small recirculation

zone just downstream of the sudden contraction may allow activated platelets to aggregate. As large variations in the wall shear stress magnitudes and distributions near the sudden contraction occurred in the simulations, the prediction of blood damage or platelet aggregation near such features must be carefully validated before its clinical impact can be determined.

A brief summary of CFD "Best Practices" identified in this study, in addition to those found in our previous report,³¹ can be found in the Appendix. Note that computational modeling is not required in device premarket notifications and applications submitted to the US FDA. However, modeling may play a useful role as part of a device submission when the goals of the study are carefully designed within a regulatory context. Despite our use of turbulence models to help organize the data presented herein, we do not endorse or recommend the use of any particular turbulence model over any other.

Study Limitations

All the limitations identified in our previous report apply.³¹ In addition, we note that the 2D PIV derived velocities were measured from only one plane in the nozzle; thus any flow asymmetries were not fully characterized. Also, for Figure 5, only the asymmetry from one plane was calculated for each 3D simulation (an example of looking at multiple planes is shown in Figure 10). Thus in both experimental and computational cases, any out-of-plane asymmetry (that is symmetric within the plane) may have led only to a reduction in the calculated flow rate (as in Figure 4), rather than to a flow asymmetry < 1.0 (as in Figure 5). This demonstrates the indeterminacy of the azimuthal position of an asymmetry in both computations and experiment. Despite these limitations, it is clear that the experimental asymmetries that were observed were much smaller than those seen in some of the simulations.

We did not attempt to use an error metric in this study, because errors were highly

dependent on location in our previous analysis.³¹ Error metrics have their uses, and we recommend they be employed in, e.g., determining the best combination of simulation parameters (i.e., sensitivity analysis) per the methods described by Oberkampf and Barone.²⁸

In the PIV experiments, larger than expected 95% confidence intervals were observed in some locations at most Reynolds numbers (Figure 6 – Figure 9), due to a combination of factors: 1) errors in the inlet flow rate (especially in one experiment) which changed the character of the flow, especially in the inlet and outlet regions; 2) optical interference by the forward facing step at the sudden contraction; 3) minor asymmetries in the diffuser geometry; and 4) difficulties in accurate velocity measurement near the nozzle walls. In the latter case, experimental WSS measurements in the throat region were difficult to measure reliably due to issues such as optical interference, inadequate pixel resolution and large velocity gradients near wall, and so were omitted in this paper. A future report will focus on developing better near-wall measurement algorithms to improve the accuracy of WSS measurements.

Future work

The goal of this study is to identify issues with and provide information on the use of CFD in regulating medical devices. We are currently using this information in the development of regulatory guidance for the reporting of computational studies to the FDA. As members of a number of standards groups (e.g., ASME V&V 40 for Medical Devices), we will provide any knowledge gained from this study to the standards-developing community.

As these studies are published, all of the experimental and computational data from this project will be posted at <https://fdacfd.nci.nih.gov>, so as to be available to anyone who wishes to use it for further development. We plan to run additional experimental and computational interlaboratory studies in the future. Please visit the website or contact us for more information.

Appendix - Best Practices (Continued from Reference #31)

Additional CFD "Best Practices" identified in this study are listed below. These are not necessarily all-inclusive, nor do they guarantee an accurate simulation.

18. Asymmetric or disturbed flow can occur in areas of decelerating flow (adverse pressure gradients), both in computations and experimental data. Such disturbances may occur in laminar, transitional, or turbulent regimes. These disturbances may be truly physically present, or they may be spurious and artifactual, particularly in numerical computations. Validation in these areas is challenging because the nature and origin of these disturbances may differ subtly among bench experiments, computer simulations, animal models, and the clinical setting. True physical asymmetries will not be accurately computed if an axisymmetric simulation is run, or may not be accurately captured if the entire flow volume or flow regime is not adequately sampled both in a simulation and/or experimental setting. As stated by Oberkampf et al.:²⁹ "When grids are sufficiently refined, completely new processes or characteristics on the smaller spatial scales can develop. It is not uncommon that a steady flow field can become unsteady as the grid is refined and very small-scale phenomena can develop that did not exist on the coarser grids."
19. Shear stresses near corners, edges, and walls are difficult to model accurately and to validate experimentally, especially when turbulence or transition is involved. Mesh refinement studies near corners (or modeling corners with their measured radii) is usually beneficial. Adequate validation may require advanced experimental techniques.^{12,19,22,24,33}
20. Modeling a spatial transition from laminar to turbulent flow poses many numerical

challenges. Some success is possible by advanced Reynolds-averaged Navier Stokes (RANS) turbulence models, such as the Shear Stress Transport models or dynamic hybrid RANS/Large Eddy Simulation models.² More sophisticated non-RANS models (e.g., large eddy simulations) may have utility here,⁹ but have yet to be fully explored in the medical device field due to their higher computational cost.

21. A basic understanding of the underlying numerical algorithms of post-processing is essential. Data extraction/interpolation needs to be carefully performed to prevent non-physical results, as demonstrated by non-zero velocities at (and beyond) the wall of the sudden contraction observed in some simulations.

Acknowledgements

We recognize and appreciate the support of the worldwide CFD community. In particular, the authors wish to thank our study participants: Yared Alemu, K. Amano, J. Ashton, Mehdi Behbahani, Catrin Bludszuweit-Philipp, Danny Bluestein, Parnian Boloori-Zadeh, Alistair Brown, Scott Corbett, Julien de Charentenay, D. de Zelicourt, Wade Dummer, K. Fraser, Leonid Goubergrits, Kurt Graichen, Linden Heflin, Darren Hitt, Marcus Hormes, Marc Horner, Xueying Huang, S. Krishnan, S. Kühne, Patricia Lawford, Ming Li, Z. Li, William Louisos, Takehisa Mori, Alex Medvedev, Joerg Mueller, Sei Murakami, Mariagrazia Pilotelli, M. Polster, N. Reuel, T. Schauer, E. Sirois, Ken Solen, Ulrich Steinseifer, Wei Sun, S. Takahashi, Masaaki Tamagawa, K. Tan, Dalin Tang, Ertan Taskin, Z. Teng, R. Toyao, Dan White, Z. Jon Wu, M. Xenos, and Ajit Yoganathan. This study was supported by the Food & Drug Administration's [Critical Path Initiative](#) Program. The mention of commercial products, their source, or their use in connection with material reported herein is not to be construed as either an actual or implied endorsement of such products by the U.S. Department of Health and Human Services.

Conflict of Interest Statement

None.

List of Tables

Table 1. Downstream Symmetry: Model parameters of two simulations

at $Re = 6500$ shown in Figure 10.

Table 2. Details of wall shear stress (WSS) at sudden contraction for seven selected SST studies

(all performed with Code A, as shown in Figure 12, top panel), at $Re = 3500$.

Table 1. Downstream Symmetry: Model parameters of two simulations
at $Re_t = 6500$ shown in Figure 10.

Parameter	Simulation 1	Simulation 2
Code	Code A	Code A
Turbulence Model	SST	SST
Z coordinate of Inlet	-0.12	-0.06
Z coordinate of Outlet	0.18	0.30
Total Number of Cells	6.6×10^5	13.4×10^5
Dominant Cell Type	Hex	Hex
Wall Functions	Standard wall functions	Automatic
Time Integration	Transient (time step = 9.5×10^{-4})	Steady
Upstream Velocity Profile	Turbulent Profile	Parabolic Profile
Outlet Boundary Condition	Averaged pressure = 0	Not given
Self-ascribed expertise	Expert	Beginner
Flow Symmetry within Diffuser	Asymmetric	Symmetric

Table 2. Details of wall shear stress (WSS) at sudden contraction for seven selected SST studies (all performed with Code A, as shown in Figure 12, top panel), at $Re_t = 3500$.

Data from File Header	Plot # in Figure 12, top panel, Code A						
	1	2	3	4	5	6	7
Mesh Type	3D	3D	3D	3D	Axisym.	Axisym.	Axisym.
Cell Type	Hexahedral	Hexahedral	Hexahedral	Tetrahedral	Quadrilateral	Quadrilateral	Triangle
Experience (1=novice, 10=expert)	8	2	4	4	6	10	7
Inlet Length (m)	-0.120	-0.060	-0.090	-0.250	-0.298	-0.090	-0.180
Outlet Length (m)	0.183	0.303	0.120	0.313	0.270	0.153	0.220
#Cells	661200	1339392	2998272	1897091	20486	130232	342450
Cell Minimum Volume (m³)	1.20E-12	1.22E-13	6.09E-11	3.23E-13	4.40E-15	6.00E-11	3.95E-15
Cell Maximum Volume (m³)	3.10E-10	2.27E-10	1.89E-13	9.01E-09	2.20E-10	7.49E-08	3.85E-11
Turbulence Model	SST	SST	SST	SST	SST*	SST	SST
Turbulence Wall Functions	standard	automatic	standard	automatic	none	standard	none
Time Integration	transient	steady	steady	steady	steady	steady	steady
Max Normalized WSS	1.64	6.94	1.08	2.98	16.10	1.07	21.51
z coordinate of minimum WSS (m)	0.00346	0.00675	0.00275	0.00047	0.00400	0.00400	0.00620

*Study #5 specified "RANS k-omega SST" in file header; all others specified "SST" or "Shear Stress Transport"

List of Figures

Figure 1. Nozzle specifications: a) dimensions of nozzle (inlet and outlet lengths unspecified); b) cross-sectional cuts defined for data submission for the Conical Diffuser.

Figure 2. Axial velocity along nozzle centerline, normalized to inlet flow rate (see text): a) $Re_t = 500$; b) $Re_t = 2000$; c) $Re_t = 3500$; d) $Re_t = 6500$. Lines are CFD with color and style representing the turbulence model used. Experimental data (symbols) are plotted as the mean \pm 95% confidence interval ($n = 4$). In (a), $Re_t = 500$, laminar CFD results labeled 1, 3, and 5 were reported to be axisymmetric, with triangular elements. Laminar CFD results labeled 2 and 4 were reported to be 3D tetrahedral.

Figure 3. Wall pressure (main figures) referenced to value at $z = 0.09032$ m (red lines over nozzle outlines): a) $Re_t = 500$; b) $Re_t = 2000$; c) $Re_t = 3500$; d) $Re_t = 6500$. Lines are CFD results plotted by families of turbulence model used. Experimental data (symbols) from wall tap measurements are plotted as the mean \pm 95% confidence interval ($n = 3$). Inset plots are corresponding CFD pressures along centerline also compared to experimental wall tap measurements. Panel e) is a contour plot of one simulation at $Re_t = 3500$, showing a localized low pressure zone adjacent to wall just downstream of sudden contraction.

Figure 4. Experimental and simulated flow rates in Conical Diffuser: a) $Re_t = 500$; b) $Re_t = 2000$; c) $Re_t = 3500$; d) $Re_t = 6500$. Lines are calculated from CFD results plotted by families of turbulence model used. Symbols are calculated from experimental PIV measurements. Dotted black lines are the theoretical flow rates calculated from the Re_t .

Figure 5. Flow rate asymmetry calculated from axial velocities. Lines are calculated from CFD axial velocities (3D simulations only), plotted by families of turbulence model used. Symbols are calculated from experimental axial velocities. a) $Re_t = 500$; b) $Re_t = 2000$; c) $Re_t = 3500$; d)

$Re_t = 6500$.

Figure 6. Normalized axial velocity profiles for throat Reynolds number = 500: a) $z = -0.024$ m (nozzle walls are at radial locations -0.006 and 0.006 m), b) $z = -0.004$ m, c) $z = 0.0$ m (nozzle walls are at radial locations -0.002 and 0.002 m), d) $z = 0.004$ m, e) $z = 0.032$ m, f) $z = 0.048$ m, g) $z = 0.056$ m, h) $z = 0.072$ m, and i) $z = 0.100$ m. Lines are CFD with color and style representing the turbulence model used. The experimental data (symbols) are plotted as the mean \pm 95% confidence interval ($n = 4$). Simulations with conservation of mass errors $> 10\%$ upstream of the conical diffuser were omitted.

Figure 7. Normalized axial velocity profiles for throat Reynolds number = 2000: a) $z = -0.024$ m, b) $z = -0.004$ m, c) $z = 0.0$ m, d) $z = 0.004$ m, e) $z = 0.032$ m, f) $z = 0.048$ m, g) $z = 0.056$ m, h) $z = 0.072$ m, and i) $z = 0.100$ m. Lines are CFD with color and style representing the turbulence model used. The experimental data (symbols) are plotted as the mean \pm 95% confidence interval ($n = 4$). Simulations with conservation of mass errors $> 10\%$ upstream of the conical diffuser were omitted.

Figure 8. Normalized axial velocity profiles for throat Reynolds number = 3500: a) $z = -0.024$ m, b) $z = -0.004$ m, c) $z = 0.0$ m, d) $z = 0.004$ m, e) $z = 0.032$ m, f) $z = 0.048$ m, g) $z = 0.056$ m, h) $z = 0.072$ m, and i) $z = 0.100$ m. Lines are CFD with color and style representing the turbulence model used. The experimental data (symbols) are plotted as the mean \pm 95% confidence interval ($n = 4$). Simulations with conservation of mass errors $> 10\%$ upstream of the conical diffuser were omitted.

Figure 9. Normalized axial velocity profiles for throat Reynolds number = 6500: a) $z = -0.024$ m, b) $z = -0.004$ m, c) $z = 0.0$ m, d) $z = 0.004$ m, e) $z = 0.032$ m, f) $z = 0.048$ m, g) $z = 0.056$ m, h) $z = 0.072$ m, and i) $z = 0.100$ m. Lines are CFD with color and style representing the turbulence

model used. The experimental data (symbols) are plotted as the mean \pm 95% confidence interval ($n = 4$). Simulations with conservation of mass errors $> 10\%$ upstream of the conical diffuser were omitted.

Figure 10. Axial velocity profiles at $z = 0.072$ m downstream of sudden contraction (as in Figure 9g) for two 3D simulations at $Re_t = 6500$. Upper left shows normalized axial velocity profiles at four angular cuts: dashed lines, Simulation 1 (asymmetric results); solid lines, Simulation 2 (symmetric results, all of which superimpose). Upper right: comparison of user-supplied (hexahedral) mesh plots for same two simulations. Bottom row: comparison of user-supplied images of cross-sectional cuts of axial velocities; lines refer to placement of profiles in upper left plot. Refer to Table 1 for comparison of simulation parameters.

Figure 11. Wall shear stress from computations as a function of axial coordinate, z : a) $Re_t = 500$; b) $Re_t = 2000$; c) $Re_t = 3500$; d) $Re_t = 6500$. Lines are CFD results plotted against turbulence model used. Simulations with conservation of mass errors $> 10\%$ upstream of the conical diffuser are omitted. In panel a, all points are shown regardless of azimuth, θ . In panels b, c, and d, only a subset of points are shown for clarity; some CFD simulations at higher Re_t had a wide variation of WSS with azimuth, due to asymmetric flow.

Figure 12. Wall shear stress (WSS) downstream of sudden contraction for SST computations at $Re_t = 3500$, for CFD codes A (top) and B (bottom), normalized to the value at $z = 0.015$ for clarity. Symbols indicate 3D simulations where submitted WSS values were not uniform as a function of θ at a single z location. *TF = Transitional flow option enabled.

References

1. Apsley DD, Leschziner MA. Advanced turbulence modelling of separated flow in a diffuser. *Flow Turbul Combust*. 1999;63:81-112.
2. Bhushan S, Walters DK. A dynamic hybrid Reynolds-averaged Navier Stokes–Large eddy simulation modeling framework. *Phys Fluids*. 2012;24:1-7.
3. Bhushan S, Walters DK, Burgreen GW. Laminar, turbulent, and transitional simulations in benchmark cases with cardiovascular device features. *Cardiovasc Eng Technol*. 2013; DOI: 10.1007/s13239-013-0155-5.
4. Charonko J, Karri S, Schmieg J, Prabhu S, Vlachos P. In vitro, time-resolved PIV comparison of the effect of stent design on wall shear stress. *Ann Biomed Eng*. 2009;37:1310-21.
5. Charonko J, Karri S, Schmieg J, Prabhu S, Vlachos P. In vitro comparison of the effect of stent configuration on wall shear stress using time-resolved particle image velocimetry. *Ann Biomed Eng*. 2010;38:889-902.
6. Chen Z, Fan Y, Deng X, Xu Z. A new way to reduce flow disturbance in endovascular stents: a numerical study. *Artif Organs*. 2011;35:392-7.
7. Cherdrone W, Durst F, Whitelaw JH. Asymmetric flows and instabilities in symmetric ducts with sudden expansions. *J Fluid Mech*. 1978;84:13–31.
8. De Bartolo C, Nigro A, Fragomeni G, Colacino FM, Wang D, Jones CC, Zwischenberger J. Numerical and experimental flow analysis of the Wang-Zwische double-lumen cannula. *ASAIO J*. 2011;57:318-27.
9. Delorme YT, Anupindi K, Frankel SH. Large eddy simulation of FDA’s idealized medical device. *Cardiovasc Eng Technol*. 2013; DOI: 10.1007/s13239-013-0161-7.

10. Down, LA. 2011. Computational investigations of red blood cell mechanical trauma and of diseased renal artery hemodynamics. Ph.D. thesis. University of Oklahoma.
11. Durst F, Melling A, Whitelaw JH. Low Reynolds number flow over a plane symmetric sudden expansion. *J Fluid Mech.* 1974;64:111–128.
12. Etebari A, Vlachos PP. Improvements on the accuracy of derivative estimation from DPIV velocity measurements. *Exp Fluids.* 2005;39:1040-50.
13. Fung YC. *Biomechanics: Circulation.* 2nd ed. New York: Springer; 1997.
14. Giridharan GA, Lederer C, Berthe A, Goubergrits L, Hutzenlaub J, Slaughter MS, Dowling RD, Spence PA, Koenig SC. Flow dynamics of a novel counterpulsation device characterized by CFD and PIV modeling. *Med Eng Phys.* 2011;33:1193-202.
15. Goubergrits L, Osman J, Affeld K. First experience with an FDA critical path initiative: CFD and hemolysis. In: *Proceedings of the XXXVI Annual ESAO Congress.* Compiègne, France; 2009. p. 398.
16. Hariharan P, Giarra M, Reddy V, Day S, Manning KB, Deutsch S, Stewart SFC, Myers MR, Berman MR, Burgreen GW, Paterson EG, Malinauskas RA. Multilaboratory particle image velocimetry analysis of the FDA benchmark nozzle model to support validation of computational fluid dynamics simulations. *J Biomech Eng.* 2011;133:041002.
17. Heflin LA, Papavassiliou DV, O'Rear EA. Simulation of hemolysis experiments: relating hemolysis and turbulent kinetic energy dissipation. *Biomedical Engineering Society Annual Meeting, Pittsburgh, PA, Oct. 7-10, 2009.*
18. Hinds MT, Park YJ, Jones SA, Giddens DP, Alevriadou BR. Local hemodynamics affect monocytic cell adhesion to a three-dimensional flow model coated with E-selectin. *J*

- Biomech. 2001;34:95-103.
19. Hochareon P, Manning KB, Fontaine AA, Tarbell JM, Deutsch S. Wall shear-rate estimation within the 50cc Penn State artificial heart using particle image velocimetry. *J Biomech Eng.* 2004;126:430-7.
 20. Hund SJ, Antaki JF, Massoudi M. On the representation of turbulent stresses for computing blood damage. *Int J Eng Sci.* 2010;48:1325-1331.
 21. Iaccarino G. Predictions of a turbulent separated flow using commercial CFD codes. *J Fluid Eng-T ASME.* 2001;123:819-28.
 22. Kähler CJ, Scholz U, Ortmanns J. Wall-shear-stress and near-wall turbulence measurements up to single pixel resolution by means of long distance micro-PIV,” *Exp. Fluids*, 2006;41:327-41.
 23. Kameneva MV, Burgreen GW, Kono K, Repko B, Antaki JF, Umezu M. Effects of turbulent stresses upon mechanical hemolysis: experimental and computational analysis. *ASAIO J.* 2004;50:418-23.
 24. Karri S, Charonko J, Vlachos PP. Robust wall gradient estimation using radial basis functions and proper orthogonal decomposition (POD) for particle image velocimetry (PIV) measured fields. *Meas Sci Technol.* 2009;20:045401-1-045401-14.
 25. Kaufmann TA, Linde T, Cuenca-Navalon E, Schmitz C, Hormes M, Schmitz-Rode T, Steinseifer U. Transient, three-dimensional flow field simulation through a mechanical, trileaflet heart valve prosthesis. *ASAIO J.* 2011;57:278-82.
 26. Medvitz RB, Boger DA, Izraelev V, Rosenberg G, Paterson EG. Computational fluid dynamics design and analysis of a passively suspended Tesla pump left ventricular assist device. *Artif Organs.* 2011;35:522-33.

27. Nabavi M. Three-dimensional asymmetric flow through a planar diffuser: Effects of divergence angle, Reynolds number and aspect ratio. *Int Commun Heat Mass*. 2010; 37:17–20.
28. Oberkampf WL, Barone MF. Measures of agreement between computation and experiment: validation metrics. *J Comput Phys*. 2006;217:5-36.
29. Oberkampf, W. L., T. G. Trucano, and C. Hirsch. Verification validation and predictive capability in computational engineering and physics. *Appl. Mech. Rev.* 57:345–384, 2004.
30. Pekkan K, de Zélicourt D, Ge L, Sotiropoulos F, Frakes D, Fogel MA, Yoganathan AP. Physics-driven CFD modeling of complex anatomical cardiovascular flows-a TCPC case study. *Ann Biomed Eng*. 2005;33:284-300.
31. Stewart SF, Paterson EG, Burgreen GW, Hariharan P, Giarra M, Reddy V, Day SW, Manning KB, Deutsch S, Berman MR, Myers MR, Malinauskas RA. Assessment of CFD performance in simulations of an idealized medical device - results of FDA's first computational interlaboratory study. *Cardiovasc Eng Technol*. 2012;3:139-60.
32. Umezu M, Fujimasu H, Yamada T, Fujimoto T, Ranawake M, Nogawa A, Kijima T. Fluid dynamic investigation of mechanical blood hemolysis. In: Akutso T, Koyanagi H, editors. *Heart Replacement Artificial Heart 5*. Tokyo: Springer, 1996. pp. 327-35.
33. Westerweel J, Geelhoed PF, Lindken R. Single-pixel resolution ensemble correlation for micro-PIV applications. *Exp Fluids*. 2004;37:375-84
34. White AT, Chong CK. Rotational invariance in the three-dimensional lattice Boltzmann method is dependent on the choice of lattice. *Journal of Computational Physics*. 2011;230:6367-78.

35. Xenos M, Girdhar G, Alemu Y, Jesty J, Slepian M, Einav S, Bluestein D. Device Thrombogenicity Emulator (DTE)--design optimization methodology for cardiovascular devices: a study in two bileaflet MHV designs. *J Biomech.* 2010;43:2400-9.
36. Yang XC, Zhang Y, Gui XM, Hu SS. Computational fluid dynamics-based hydraulic and hemolytic analyses of a novel left ventricular assist blood pump. *Artif Organs.* 2011 Apr 26. Epub ahead of print.
37. Yoshida M, Wearden PD, Dur O, Pekkan K, Morell VO. Right ventricular outflow tract reconstruction with bicuspid valved polytetrafluoroethylene conduit. *Ann Thorac Surg.* 2011;91:1235-8.
38. Yu H, Thévenin D, Janiga G. Numerical prediction of hemolysis based on computational fluid dynamics. In: *Proceedings of the ECCOMAS Thematic International Conference on Simulation and Modeling of Biological Flows (SIMBIO 2011)*. Brussels; 2011. pp. 1-4.

Figure 1
[Click here to download high resolution image](#)

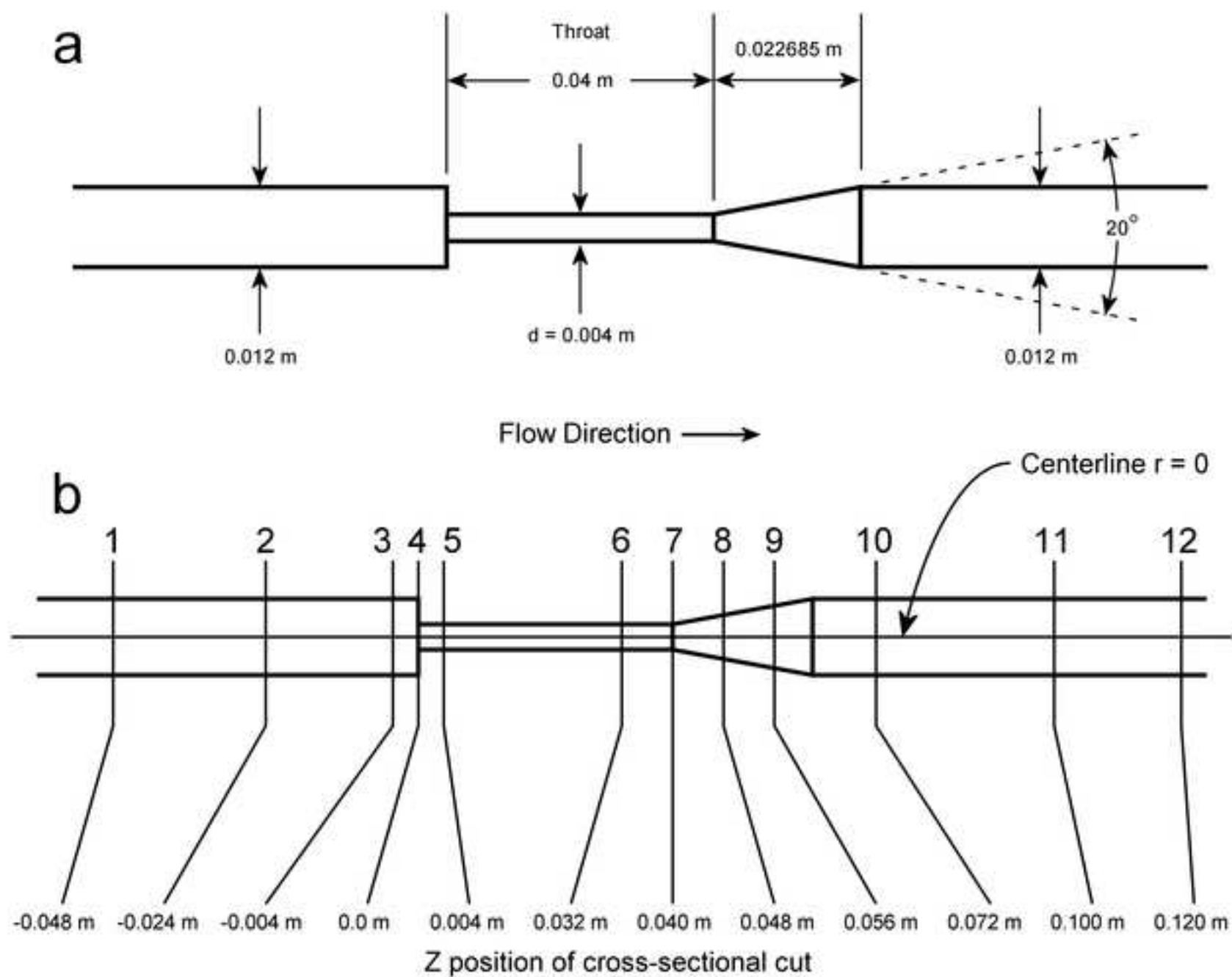


Figure 2
[Click here to download high resolution image](#)

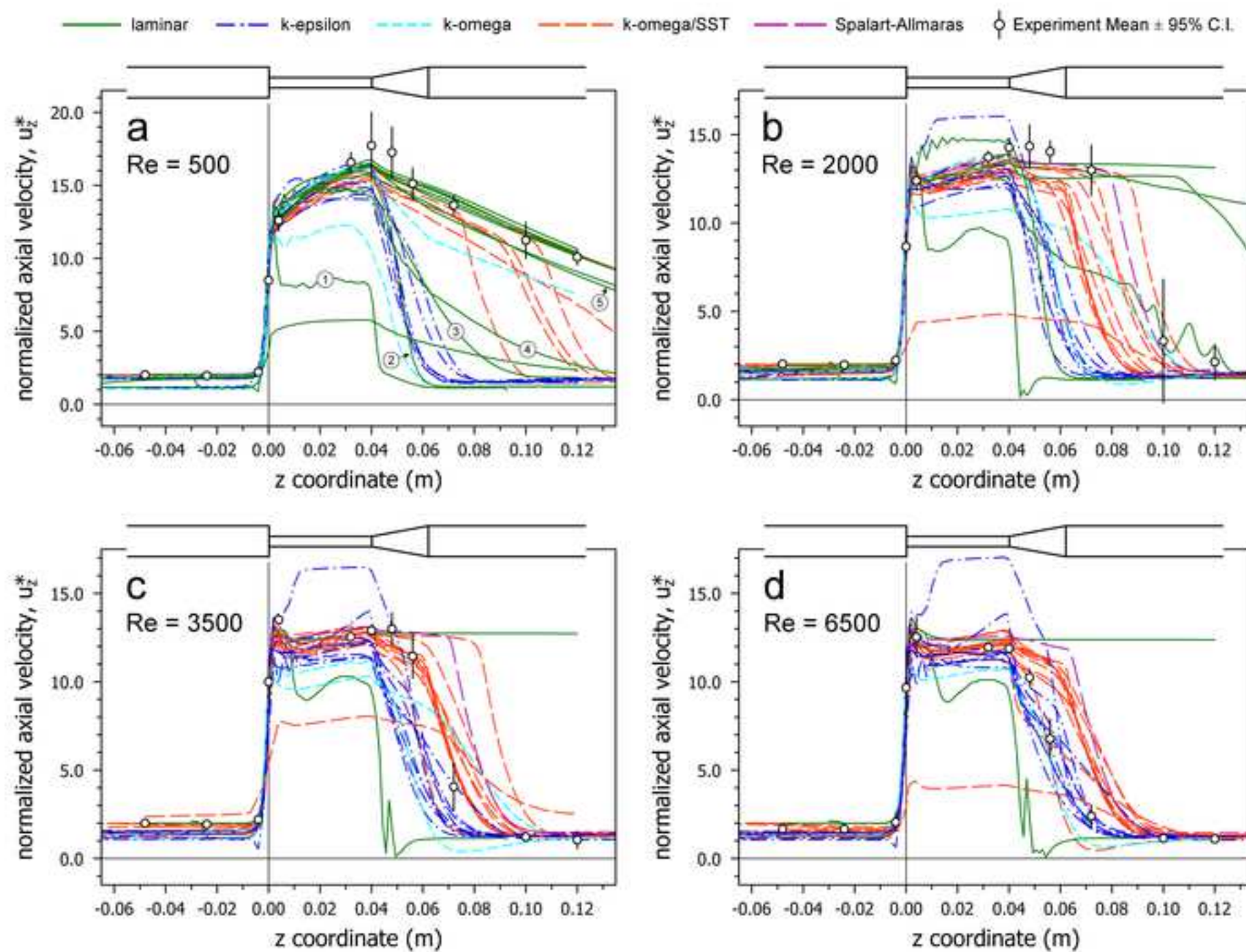


Figure 3
[Click here to download high resolution image](#)

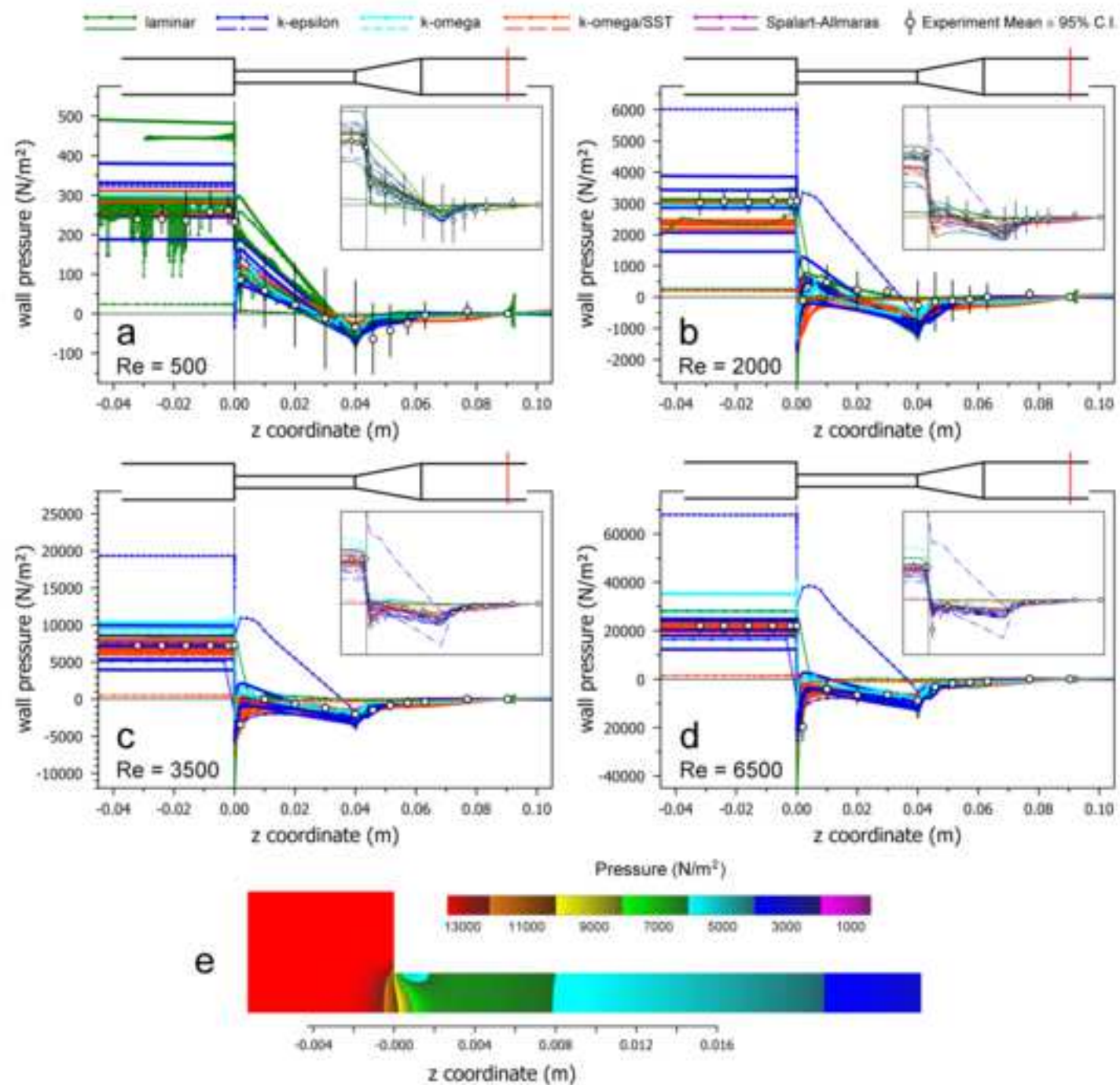


Figure 4

[Click here to download high resolution image](#)

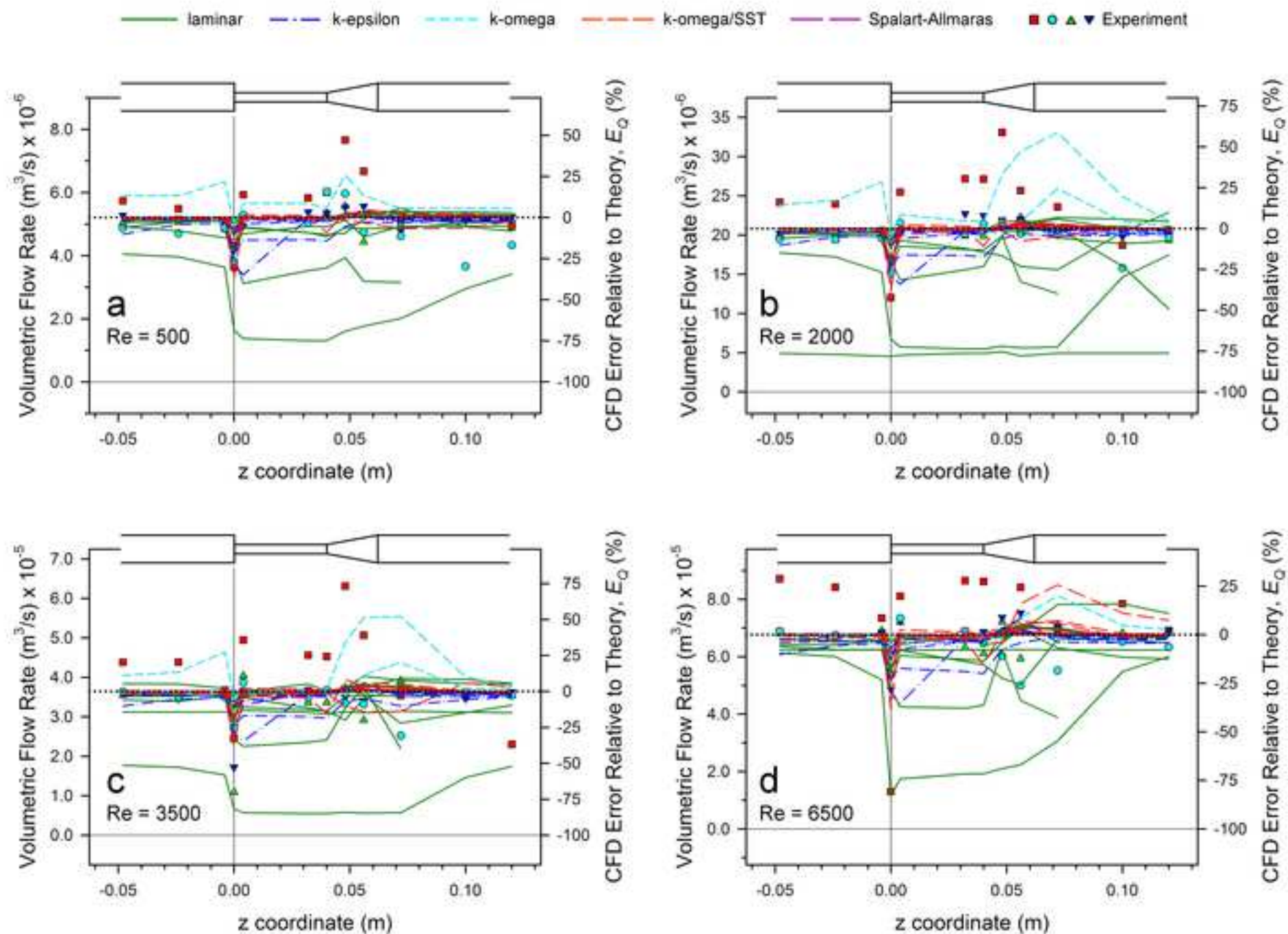


Figure 5
[Click here to download high resolution image](#)

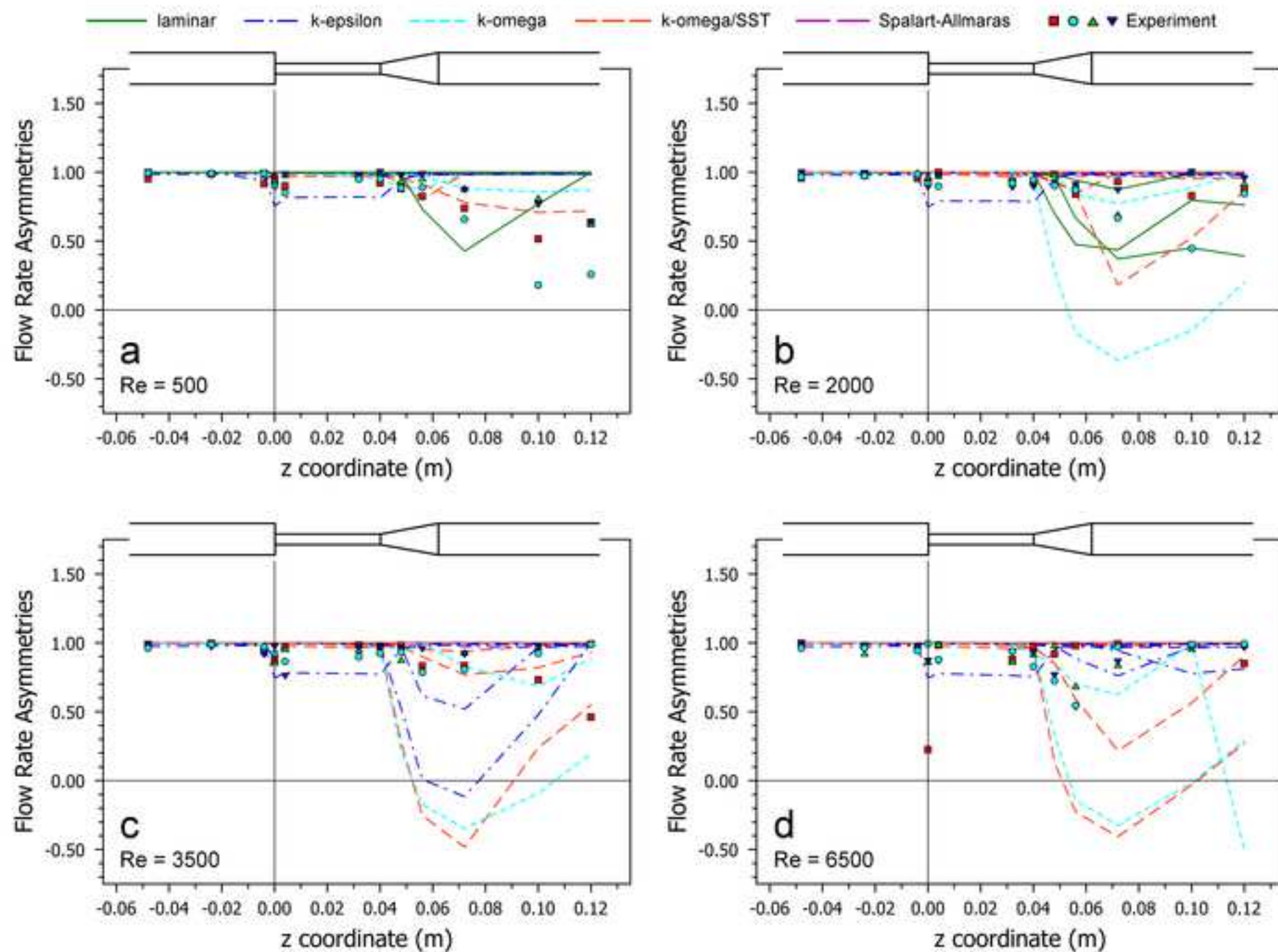


Figure 6
[Click here to download high resolution image](#)

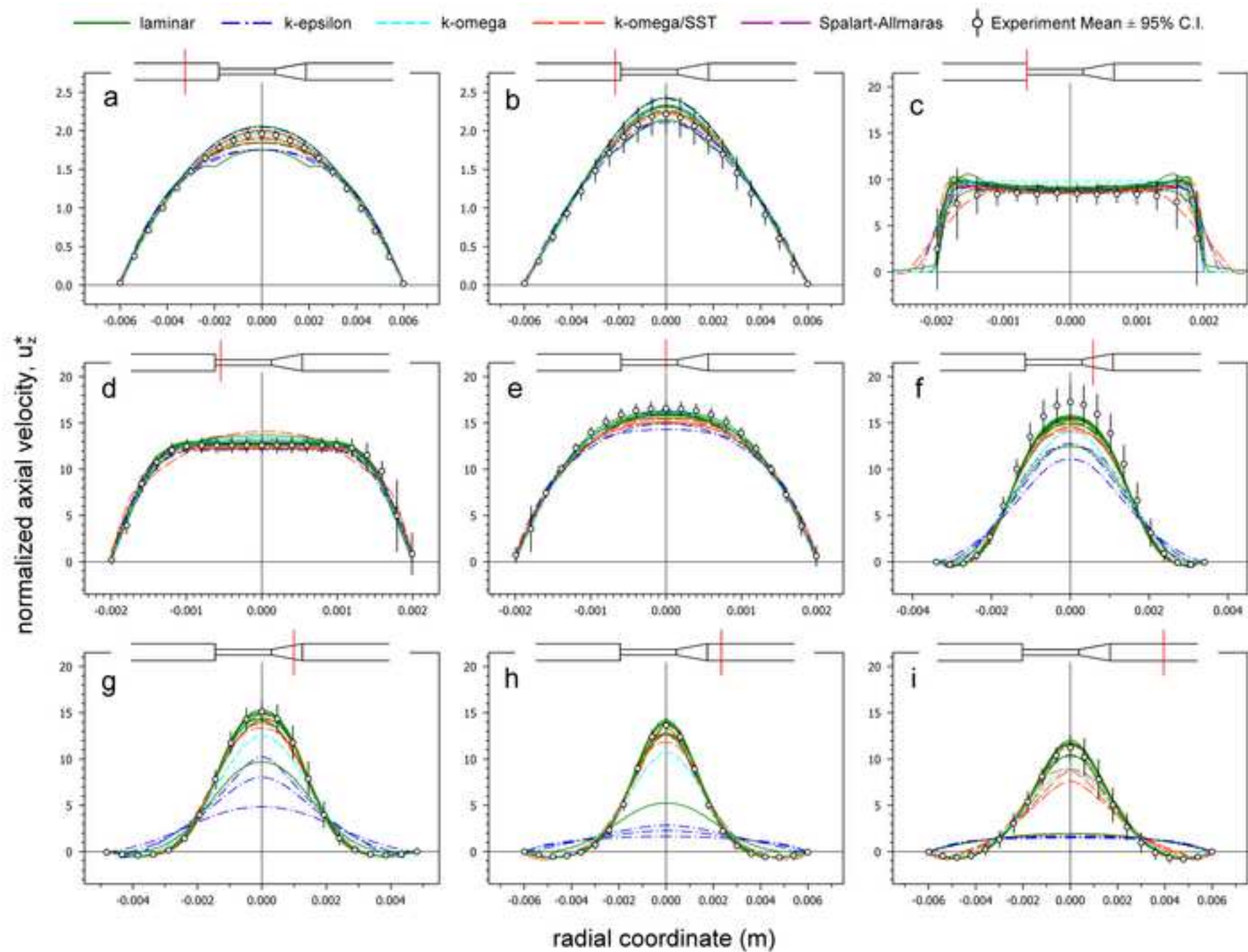


Figure 7
[Click here to download high resolution image](#)

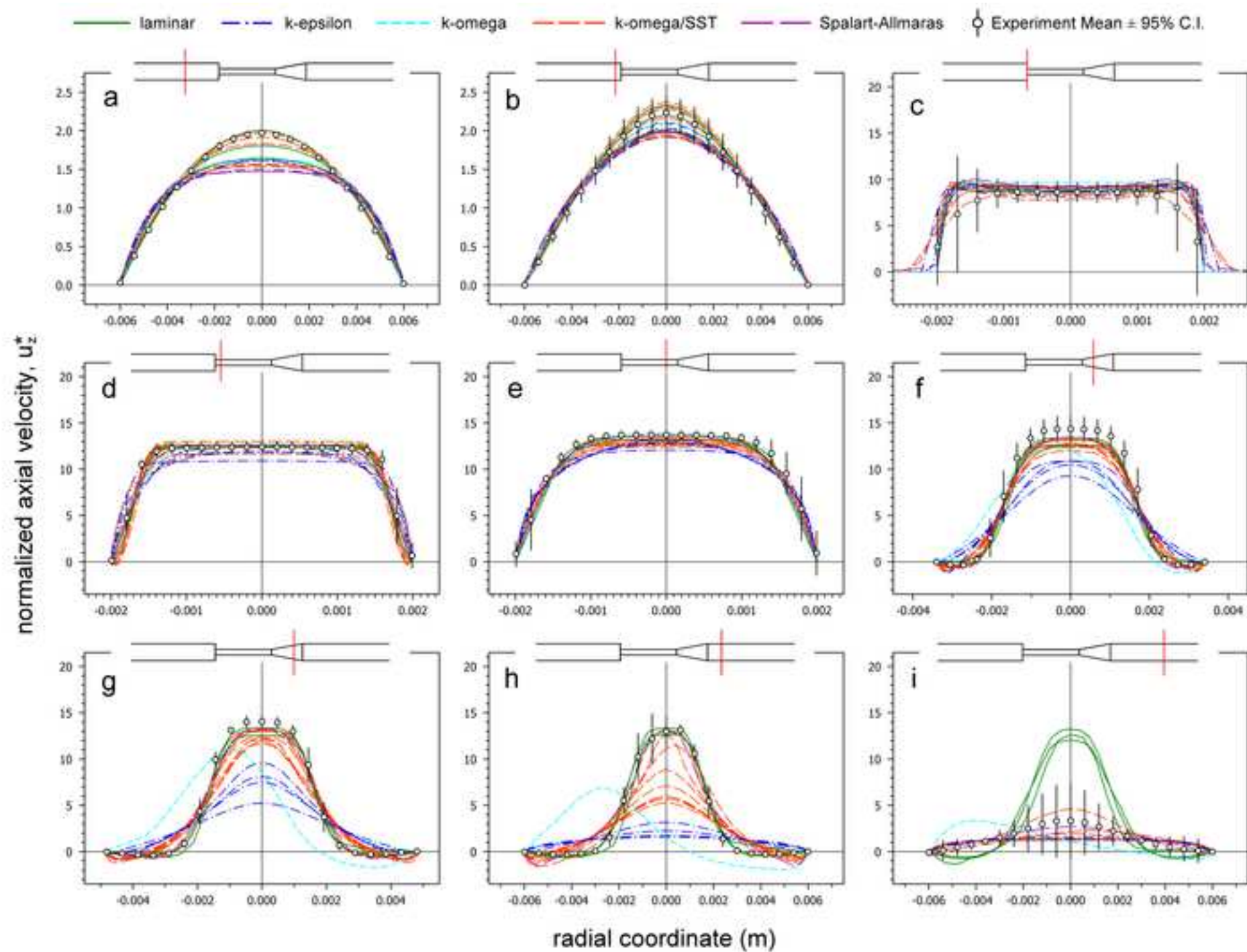


Figure 8
[Click here to download high resolution image](#)

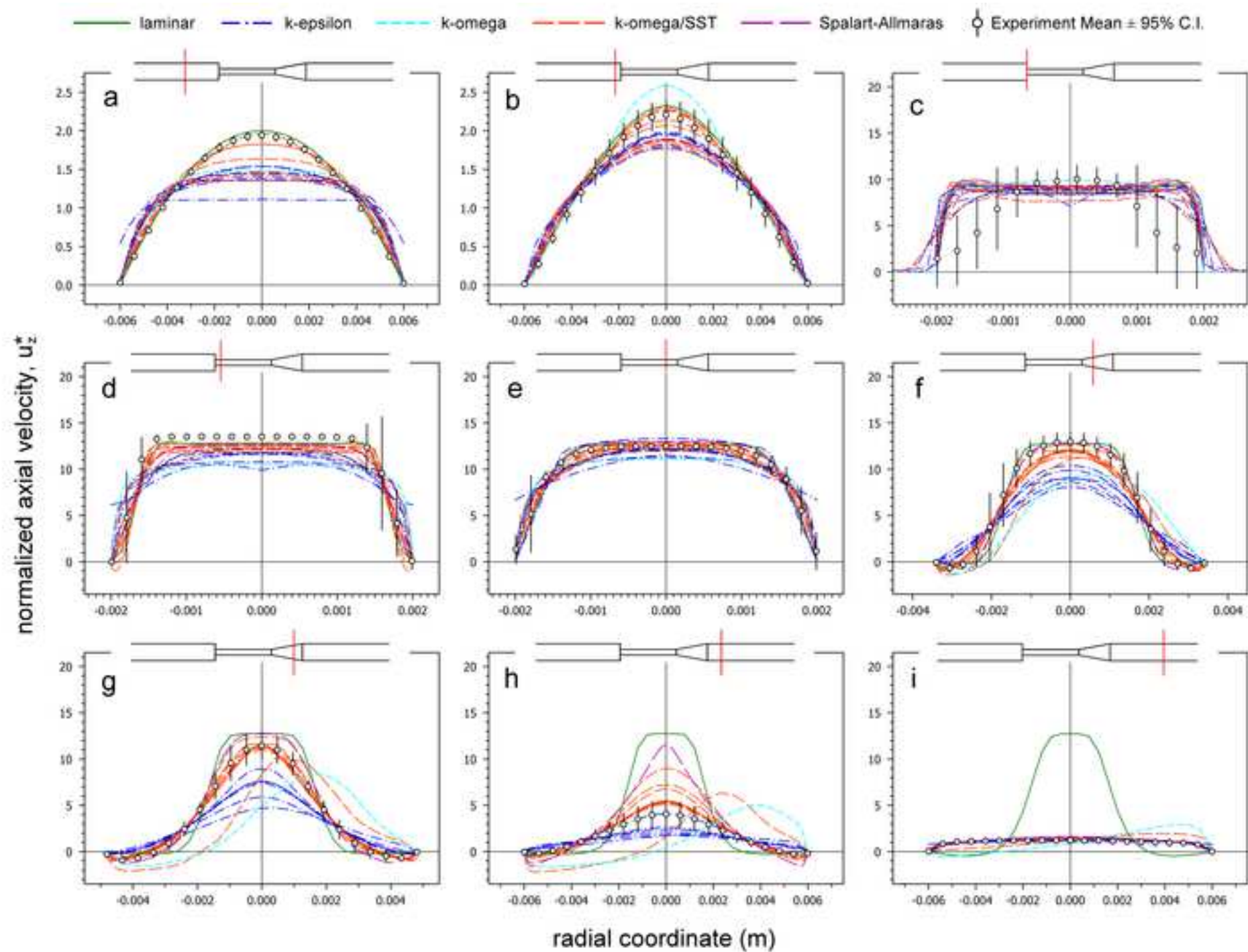


Figure 9
[Click here to download high resolution image](#)

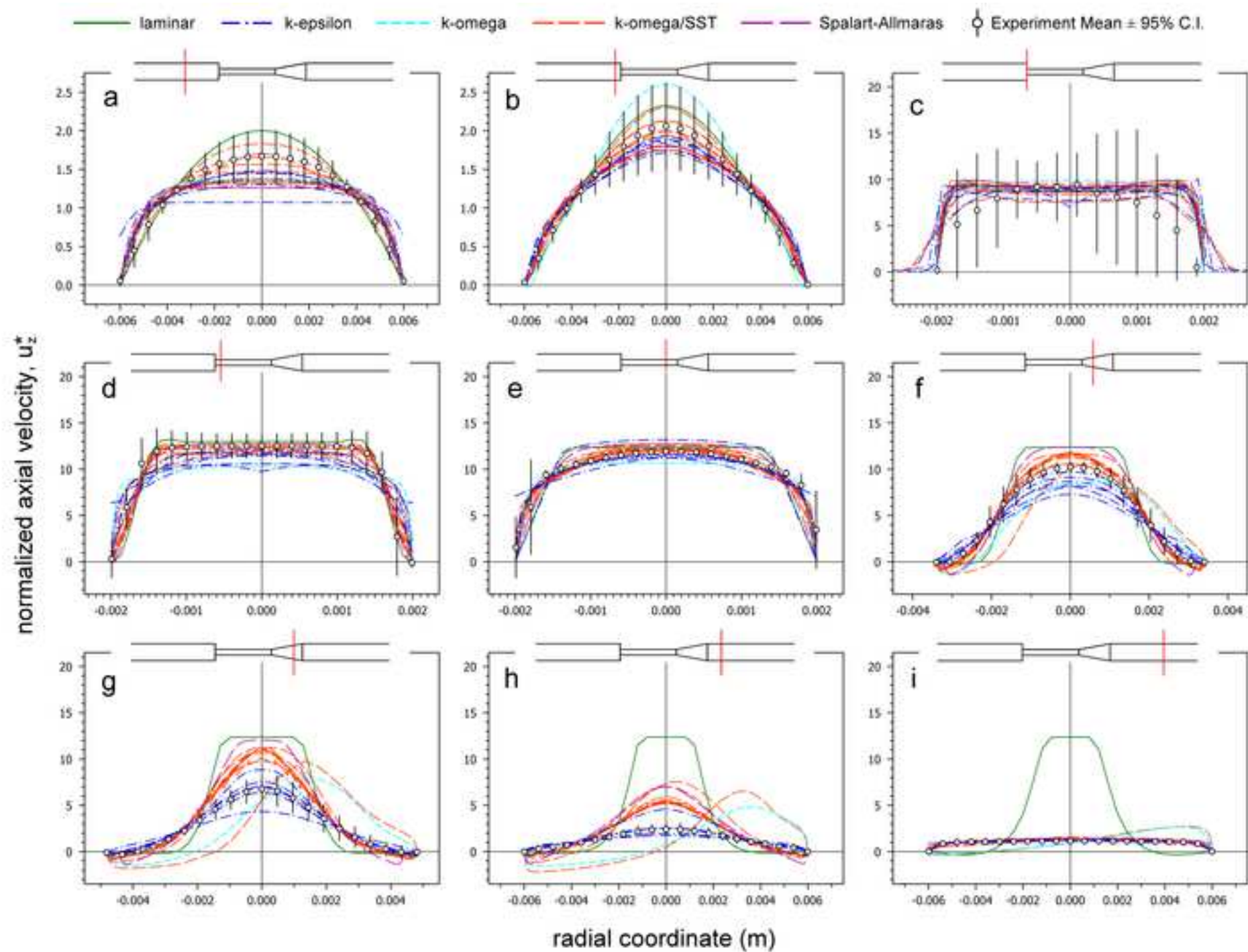


Figure 10
[Click here to download high resolution image](#)

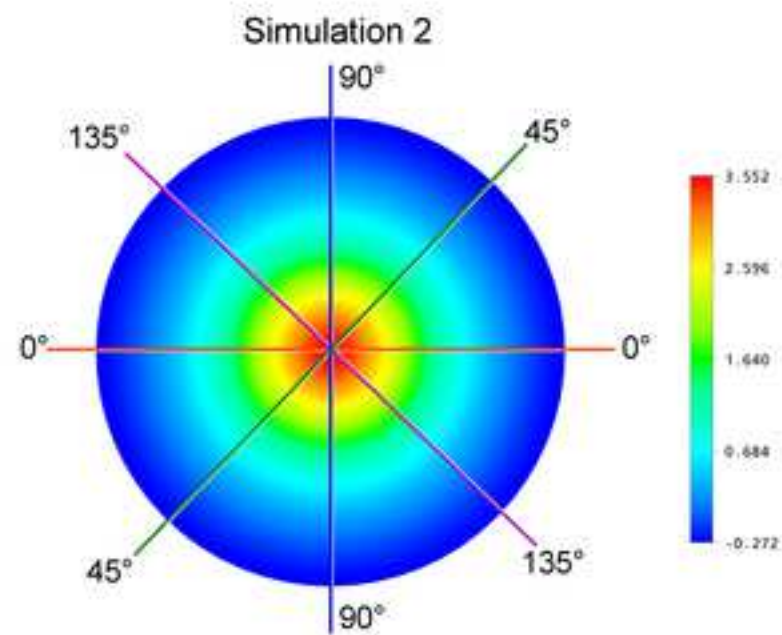
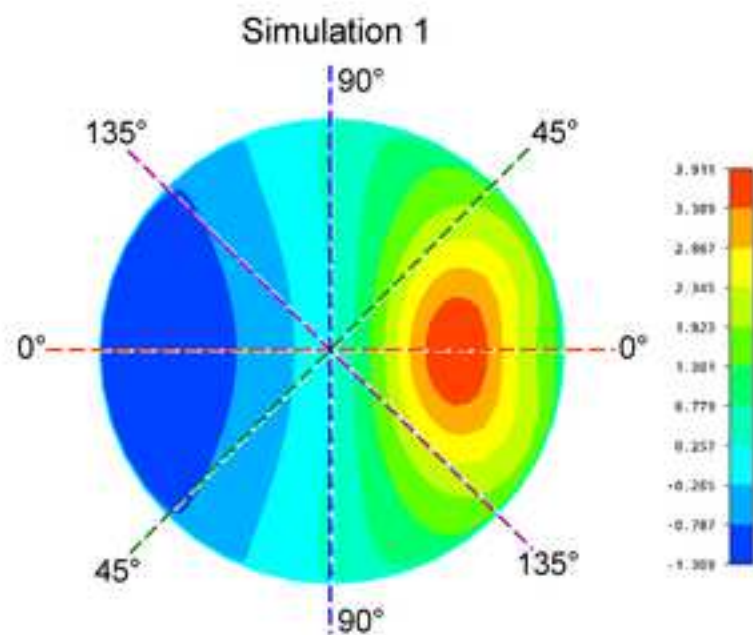
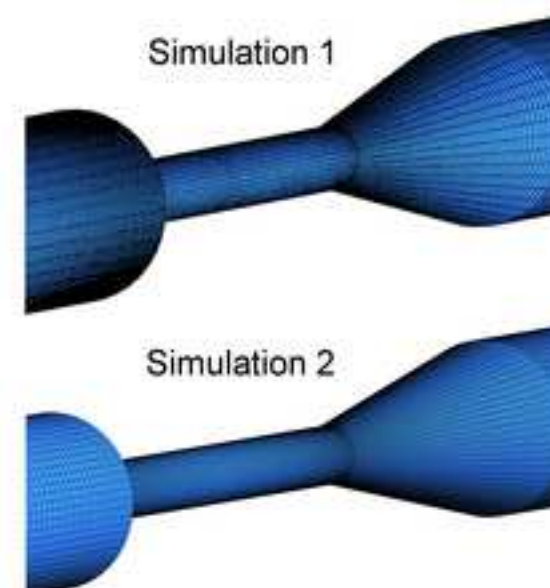
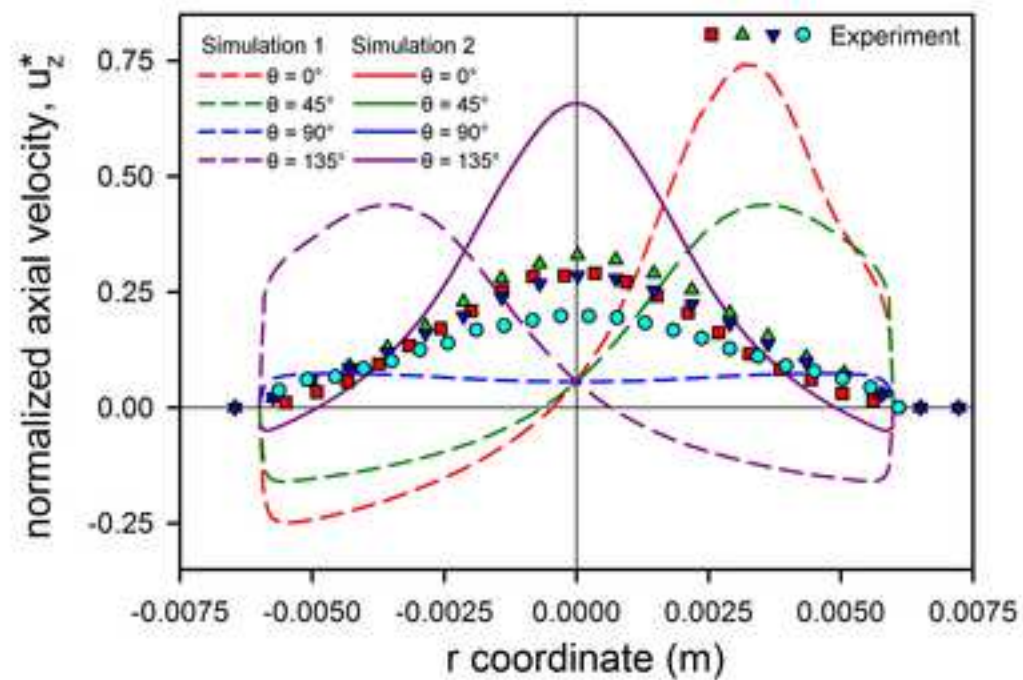


Figure 11
[Click here to download high resolution image](#)

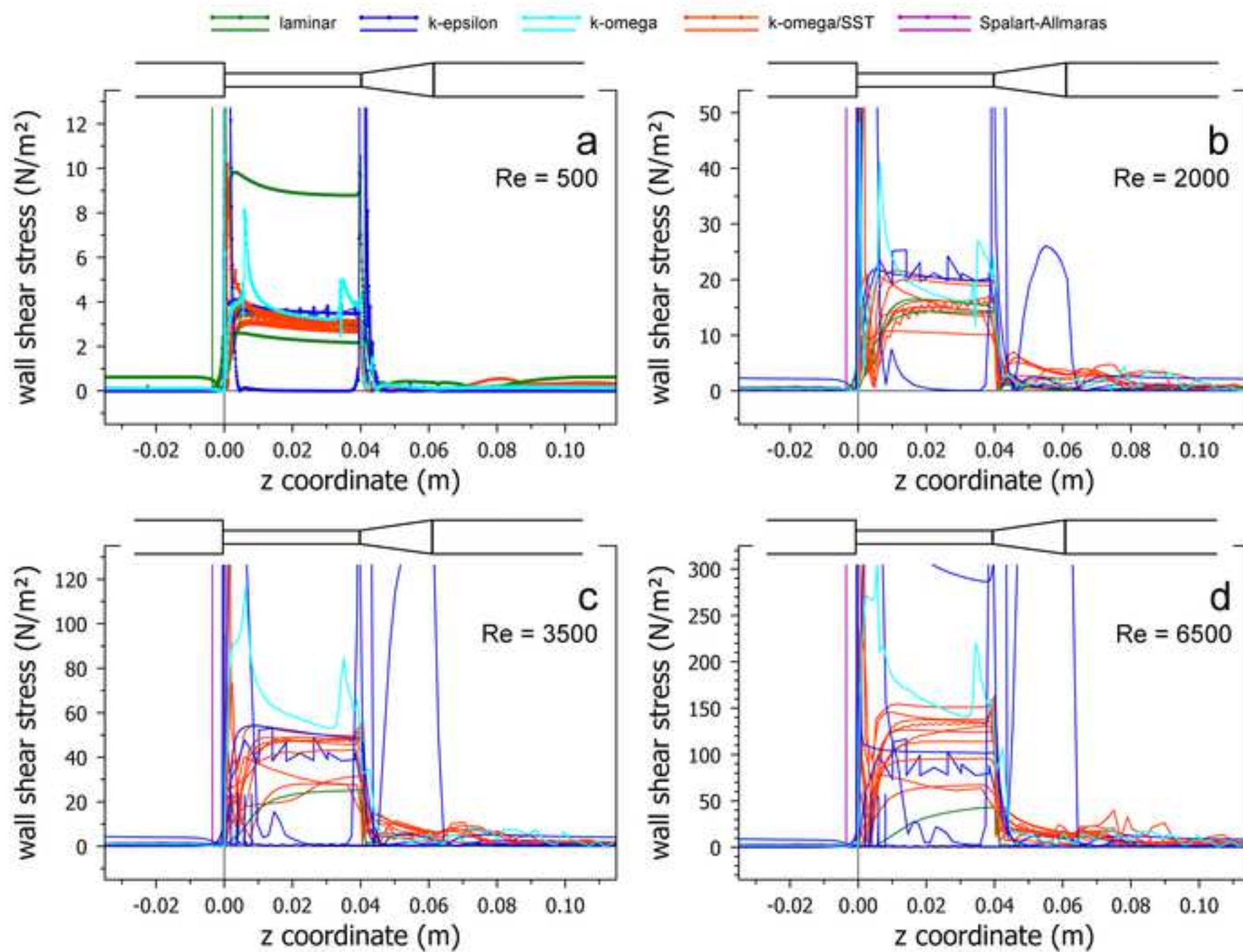
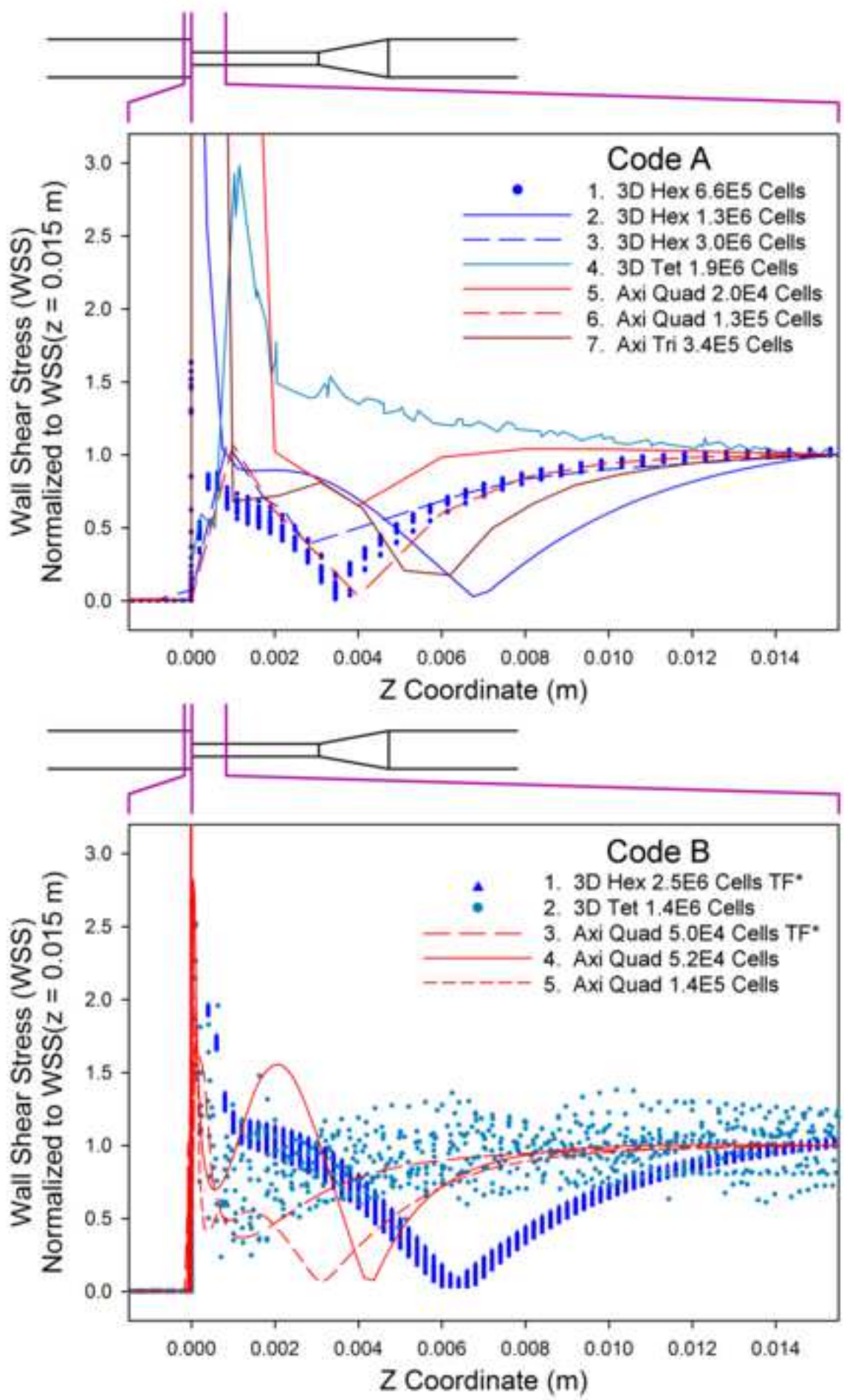


Figure 12
[Click here to download high resolution image](#)



Please wait...

If this message is not eventually replaced by the proper contents of the document, your PDF viewer may not be able to display this type of document.

You can upgrade to the latest version of Adobe Reader for Windows®, Mac, or Linux® by visiting http://www.adobe.com/go/reader_download.

For more assistance with Adobe Reader visit <http://www.adobe.com/go/acrreader>.

Windows is either a registered trademark or a trademark of Microsoft Corporation in the United States and/or other countries. Mac is a trademark of Apple Inc., registered in the United States and other countries. Linux is the registered trademark of Linus Torvalds in the U.S. and other countries.